Hybrid and quark star matter based on a nonperturbative equation of state

Konstantin Otto[1,*] Micaela Oertel[2,†] and Bernd-Jochen Schaefer[1,‡]

[1]*Institut für Theoretische Physik, Justus-Liebig-Universität Gießen, D-35392 Gießen, Germany*
[2]*LUTH, Observatoire de Paris, PSL Research University, CNRS, Université de Paris,*
5 place Jules Janssen, 92195 Meudon, France

With the recent dawn of the multimessenger astronomy era a new window has opened to explore the constituents of matter and their interactions under extreme conditions. One of the pending challenges of modern physics is to probe the microscopic equation of state (EoS) of cold and dense matter via macroscopic neutron star observations such as their masses and radii. Still unanswered issues concern the detailed composition of matter in the core of neutron stars at high pressure and the possible presence of, e.g., hyperons or quarks. By means of a nonperturbative functional renormalization group approach the influence of quantum and density fluctuations on the quark matter EoS in β-equilibrium is investigated within two- and three-flavor quark-meson model truncations and compared to results obtained with common mean-field approximations where important fluctuations are usually ignored. We find that they strongly impact the quark matter EoS.

I. INTRODUCTION

The recent clean mass determinations for two pulsars, PSR J1614 − 2230 and PSR J0348 + 0432 [1], confirm the existence of neutron stars (NS) with a mass of about—and possibly even beyond, see [2]—two solar masses. Since the NS mass and radius depend strongly on the underlying equation of state (EoS), see, e.g., the reviews [3–5], any model for the NS interior should produce an EoS leading to a maximum NS mass at least compatible with the above observations. The maximum mass is thereby most sensitive to the EoS at the highest densities. The central densities of the maximum mass configuration can reach values of about 1 fm^{-3}, well above the nuclear saturation density, $\rho_0 \sim 0.16$ fm^{-3}, and other degrees of freedom than neutrons, protons, and electrons might appear. Although additional degrees of freedom soften the EoS and thus lower the maximum mass, it has been demonstrated that the appearance of hyperons [6], mesons, or Δ-baryons [7], is not excluded by the observation of the two massive pulsars. Numerous studies demonstrate in addition the possibility of a transition to quark matter at high density in such massive stars and the formation of so-called hybrid stars [8,9]. Under the hypothesis of absolutely stable strange quark matter [10], even pure quark stars, also referred to as strange stars, might exist [11].

The onset of a new degree of freedom causes not only a reduction of the maximum mass but in general leads to smaller radii of the stars, too. For strange quark stars, the mass-radius relation is qualitatively different from neutron and hybrid stars. In particular, strange quark stars are much more compact than their neutron or hybrid counterparts since they are mainly composed of self-bound matter. Thus, observing a pulsar with a very small radius would be a strong indication for a strange quark star. However, radii are difficult to measure and the extracted values are model dependent. Presently, they have been essentially estimated from x-ray observations, see [12] for a recent review, and from the tidal deformability of GW170817 measured by the LIGO-Virgo collaboration [13–17]. The obtained values lie in the range of 10–14 km for a fiducial 1.4 $M_\odot$ star and are perfectly compatible with neutron or hybrid stars. In the near future further precise radius determinations are to be expected from the NICER mission and additional binary NS merger data from LIGO-Virgo detectors.

From a theoretical point of view, it is not possible up to now to derive the dense matter EoS from first principles over the entire range necessary for describing compact stars, neither on the hadronic nor on the quark side. Therefore simplified EoS at finite densities need to be constructed. Currently two main strategies are pursued. The first one consists in parametrizing the EoS in the unknown density domains, putting the least possible number of

*konstantin.otto@physik.uni-giessen.de
†micaela.oertel@obspm.fr
‡bernd-jochen.schaefer@theo.physik.uni-giessen.de

model assumptions. The parameters are then adjusted to existing constraints from nuclear experiments, observations and/or theoretical calculations, including attempts to extract the density dependence of the EoS directly from NS mass and radius data. Examples are the EoS by [18,19]. The second, more traditional strategy is based on modeling dense matter. It is less flexible than the aforementioned but has the advantage of allowing to track among others the matter's particle content. Although some points remain open, for instance on inhomogeneous matter in the crust, decades of considerable effort together with constraints from experimental data and theoretical calculations have led to reliable models for nuclear matter up to roughly twice the saturation density. Above this density, not only the models are less under control, but non-nucleonic degrees of freedom might appear and the situation becomes more complicated.

Hybrid EoS thereby include both hadronic as well as quark matter and are usually obtained by a combination of the corresponding EoS for both sides. The quark matter part is subject to even larger uncertainties than the hadronic one, being *per se* a nonperturbative QCD issue. It is still under development in particular at high baryonic densities and small temperatures appropriate for NS. Examples are based on perturbative QCD [20], density-dependent quark-mass models [21], Nambu–Jona-Lasinio (NJL)-models [22], quark-meson model investigations [23], Dyson-Schwinger type approaches [24], holographic [25], or quasiparticle models [26]. Lattice QCD calculations, which have allowed us to considerably improve our understanding of the EoS at low baryon chemical potentials, are afflicted by the sign problem at finite density and can thus not directly be applied to neutron stars. For the moment some models include constraints from lattice results at low chemical potentials, see, e.g., [27] or use QCD-like theories not subject to the sign problem, for instance G2-QCD [28], but much effort is still needed.

In this work an EoS for quark matter within a model based on the underlying chiral symmetry breaking of QCD is derived and the consequences for the structure of a nonrotating star are analyzed. In contrast to many previous works using the mean-field approximation, the functional renormalization group (FRG) approach is employed here to incorporate additional nonperturbative effects via quark and meson fluctuations. The considered quantum and density fluctuations are of particular importance in the vicinity of phase transitions and are usually ignored in mean-field approximations. These might be some reasons for the recent growing interest in the application of the FRG method to neutron star matter [29,30].

Moreover, a phase transition from hadronic matter to quark matter can be modeled which might be of relevance for hybrid stars. In the quark matter core of a hybrid star, strange quarks might be suppressed due to their relatively large effective mass [22,31–33]. In addition, large effective

strange quark masses often destabilize hybrid stars with a strange quark matter core, leading to gravitational collapse [22,32], such that we consider the two- and three-flavor cases separately here.

With our approach it becomes feasible to investigate the influence of quantum as well as density fluctuations on observables for neutron stars such as the mass-radius relation in a systematic manner. We will consider here nonmagnetized matter, since magnetic effects on the EoS are expected to play a minor role for pulsars [34].

The paper is organized as follows: after a brief setup of the used effective quark-meson model for quark matter, in Sec. II, three different approximations of the grand potential are presented which incorporate various contributions of certain quantum, thermal and density fluctuations. The numerical results of the phase structure are summarized in Sec. III. As input for the analysis of the mass-radius relation of a neutron star the EoS is needed. In Sec. IV various EoS for symmetric as well as for β-equilibrated and charge neutral matter are calculated and compared with a non-perturbative EoS obtained with the FRG with and without strange quarks. In addition, a phase transition from hadronic to quark matter is implemented and the parameter independent consequences are studied. The speed of sound in quark matter for various approximations is analyzed in Sec. IV A. The resulting mass-radius relations for all the used approximations are presented in Sec. IV B. We conclude in Sec. V and summarize our findings. Parameter choices and numerical details can be found in the Appendixes A and B.

II. CONSTRUCTING A NONPERTURBATIVE EOS

As mentioned above, we will be mainly concerned with determining the EoS of the quark core of a hybrid star or that of a strange star. To that end, we will consider a quark part and a leptonic part. The latter will be treated as a relativistic noninteracting Fermi gas. In the following, we focus on the quark part which will be calculated within an effective two- and three-quark flavor quark-meson model framework and we will investigate different approximations. The quark-meson model has been widely used as an effective model of low-energy QCD since it successfully incorporates dynamical chiral symmetry breaking and the generation of constituent quark masses. In contrast to NJL-type models often employed in this context, the quark-meson model used here does not implement a repulsive vector interaction channel which would stiffen the EoS [35]. We confront two different mean-field approximations of the effective potential with the results obtained within the functional renormalization group. This comparison enables a systematic and parameter independent analysis of the influence of certain quantum and density fluctuations on the EoS for vanishing temperature.

Within this first study, we neglect the possibility of diquark pairing and do not enter the discussion of the extremely rich phase structure of color superconducting

matter in the density range of neutron stars. Diquark pairing is important for transport properties, but, being a Fermi surface phenomenon, has only little influence on the equation of state we are focusing on here.

A. Quark-meson models

The quark-meson model consists of N_f flavors of constituent quarks q and dynamical (pseudo-)scalar meson fields ϕ_a encoded in the meson matrix

$$\Phi := T_a \phi_a, \quad a = 0, ..., N_f^2 - 1 \tag{1}$$

with $\phi_a := \sigma_a + i\pi_a$ and the generators T_a of the $U(N_f)$ group transformations. The model features besides the usual kinetic terms for all involved fields a Yukawa-type interaction between the quarks and mesons as well as mesonic self-interactions through the chirally invariant potential

$$U(\rho_1, ..., \rho_{N_f}), \tag{2}$$

which is in general a function of N_f independent chiral invariants

$$\rho_n = \text{Tr}[(\Phi^\dagger \Phi)^n], \quad n = 1, ..., N_f. \tag{3}$$

For two light and one heavy quark flavors, $N_f = 2 + 1$, the generators of the corresponding $U(3)$ transformations in flavor space can be chosen as the usual Gell-Mann matrices $\hat{\lambda}_a$, i.e., $T_a = \hat{\lambda}_a/2$. Omitting in the effective potential the highest chiral invariant ρ_3 whose associated coupling constant is of negative mass dimension, the three-quark flavor Euclidean Lagrangian reads

$$\mathcal{L}_{\text{qm}}^{(2+1)} = \bar{q}(\partial\!\!\!/ + gT_a(\sigma_a + i\gamma_5\pi_a))q + \text{Tr}(\partial_\mu \Phi^\dagger \partial_\mu \Phi)$$
$$+ U(\rho_1, \rho_2) - c_A \xi - c_l \sigma_l - c_s \sigma_s \tag{4}$$

wherein additionally the lowest order axial $U(1)_A$ symmetry breaking term

$$\xi := \det \Phi + \det \Phi^\dagger \tag{5}$$

and two explicit chiral symmetry breaking terms $-c_l \sigma_l - c_s \sigma_s$ have been added. We assume here a perfect $SU(2)$ isospin symmetry, such that the two lightest quark flavors *up* and *down* can be replaced by one index $l = u = d$ while the *strange* quark flavor is denoted by the index s. The relation of the singlet-octet basis (σ_0, σ_8) and the non-strange-strange basis (σ_l, σ_s) in the scalar meson sector is governed by a rotation

$$\begin{pmatrix} \sigma_l \\ \sigma_s \end{pmatrix} = \frac{1}{\sqrt{3}} \begin{pmatrix} \sqrt{2} & 1 \\ 1 & -\sqrt{2} \end{pmatrix} \begin{pmatrix} \sigma_0 \\ \sigma_8 \end{pmatrix} \tag{6}$$

such that the isospin-symmetric vacuum condensate evaluates to

$$\langle \Phi \rangle = T_0 \sigma_0 + T_8 \sigma_8 = \text{diag}\left(\frac{\sigma_l}{2}, \frac{\sigma_l}{2}, \frac{\sigma_s}{\sqrt{2}}\right). \tag{7}$$

For only two quark flavors, $N_f = 2$, the model simplifies to

$$\mathcal{L}_{\text{qm}}^{(2)} = \bar{q}\left(\partial\!\!\!/ + \frac{g}{2}(\sigma + i\gamma_5 \vec{\tau} \cdot \vec{\pi})\right)q + \frac{1}{2}(\partial_\mu \varphi)^2 + U(\rho) - c\sigma \tag{8}$$

with the three Pauli matrices $\vec{\tau}$ as generators and only one independent chiral invariant

$$\rho \equiv \rho_1 = \frac{1}{2}(\sigma^2 + \vec{\pi}^2) \tag{9}$$

in the mesonic chiral effective potential U with one scalar field σ and three pseudoscalar pions $\vec{\pi}$ summarized in $\varphi^T := (\sigma, \vec{\pi})$. Implicitly a maximal $U(1)_A$-symmetry breaking is assumed in this representation since the remaining chiral (pseudo)scalar multiplets, the η and $\vec{a}$ fields, are neglected. For more details see, e.g., [36].

The grand partition function $\mathcal{Z}$ in thermal equilibrium is defined by a path integral over the quark/antiquark and meson fields wherein the temperature is introduced via the Matsubara formalism. The Euclidean Lagrangian generally contains N_f independent quark chemical potentials μ_f which are added to the quark-meson Lagrangian in standard thermodynamic manner

$$\mathcal{L}^{(N_f)} = \mathcal{L}_{\text{qm}}^{(N_f)} + \sum_f^{N_f} \mu_f q_f^\dagger q_f. \tag{10}$$

The three quark flavor chemical potentials are not independent. Since we are interested in cold neutron star matter, we assume weak equilibrium including β-equilibrium with neutrinos freely leaving the star,

$$\mu_u = \mu - \frac{2}{3}\mu_e$$
$$\mu_d = \mu_s = \mu + \frac{1}{3}\mu_e, \tag{11}$$

where μ denotes the quark chemical potential related to baryon number, $\mu = \mu_B/3$, and μ_e the electron chemical potential which in the present case is the negative charge chemical potential. In addition, electrical charge neutrality has to be fulfilled,

$$\frac{2}{3}n_u - \frac{1}{3}n_d - \frac{1}{3}n_s - n_e = 0, \tag{12}$$

such that only one independent chemical potential remains. We choose μ as such. Note that even though the chemical

potentials introduced in Eq. (11) break isospin symmetry, we still assume only one light condensate σ_l as an approximation. This leads to equal masses $m_u = m_d = m_l$ even in isospin asymmetric matter.

Finally, the logarithm of the grand partition function yields the total grand potential which in general incorporates the thermal, density and quantum fluctuations of the quark and meson fields

$$\Omega(T,\mu) = \frac{-T \ln \mathcal{Z}}{V}. \quad (13)$$

B. Mean-field approximation

In mean-field approximation (MFA) the grand potential for the quark-meson model basically splits into a quark loop and a static meson contribution

$$\Omega(T,\mu) = \Omega_q + \Omega_m. \quad (14)$$

For $N_f = 2 + 1$ quark flavors the meson contribution Ω_m, ignoring the ρ_3 invariant, reads

$$\Omega_m^{(2+1)} = U_\chi(\rho_1, \rho_2) - c_A \xi - c_l \sigma_l - c_s \sigma_s \quad (15)$$

with the chirally symmetric meson potential $U_\chi(\rho_1, \rho_2) = m^2 \rho_1 + \lambda_1 \rho_1^2 + \lambda_2 \rho_2$ introducing in this manner a mass parameter m^2 and two quartic couplings λ_i.

For only two quark flavors the chiral potential simplifies to

$$U_\chi(\rho) = m^2 \rho + \lambda \rho^2. \quad (16)$$

The employed input parameters can be found in Appendix A.

The integration over the quark loop yields a UV finite and explicitly temperature dependent contribution

$$\Omega_q^{(2+1)} = \frac{N_c}{\pi^2} T \sum_{f=u,d,s} \int_0^\infty dp\, p^2 [\ln(1 - n_f(E_f, \mu_f, T))$$
$$+ \ln(1 - n_f(E_f, -\mu_f, T))] \quad (17)$$

with the usual Fermi-Dirac distribution functions $n_f(E_f, \mu_f, T) = 1/[1 + \exp((E_f - \mu_f)/T)]$, the quark energies $E_f = \sqrt{p^2 + m_f^2}$ and corresponding light, $m_l = g\sigma_l/2$, and strange quark masses $m_s = g\sigma_s/\sqrt{2}$. The light and the strange condensates σ_l and σ_s are the temperature and quark chemical potential dependent minima of the full thermodynamic potential. Again, for only two quark flavors the strange quark contribution in this expression is simply dropped and the light quark mass is replaced by $m_l = g\sigma/2$ with one chiral order parameter σ.

In general, the UV divergent vacuum contribution of the quark loop to the potential can be completely absorbed in the model parameters because the quark-meson model is renormalizable. Ignoring this divergent zero point part yields the standard MFA (sMFA). However, this vacuum contribution is automatically included in the fully renormalized quark flow equation,

$$\Omega_{rMFA,q}^{(2+1)} = \frac{N_c}{6\pi^2} \sum_{f=u,d,s} \int_0^\Lambda dk \frac{k^4}{E_f}$$
$$\times \left[\tanh\left(\frac{E_f - \mu_f}{2T}\right) + \tanh\left(\frac{E_f + \mu_f}{2T}\right) \right]. \quad (18)$$

In this way important vacuum fluctuations in addition to the thermal and density fluctuations from the quark loops are included in the grand potential [37]. In the following, we denote this approach by renormalized MFA (rMFA). In both mean-field approximations the fluctuations and backreactions on the mesonic sector are completely left out and the same static (tree-level) meson potential is used. However, all quark and meson fluctuations can finally be considered by applying the functional renormalization group method.

C. Functional renormalization group

As mentioned in the Introduction a suitable framework to incorporate quantum fluctuations in a consistent way is based on the nonperturbative functional renormalization group in terms of the Wetterich equation [38]

$$\partial_t \Gamma_k = \frac{1}{2} \text{Tr}[\partial_t R_k (\Gamma_k^{(2)} + R_k)^{-1}] \quad (19)$$

with the RG time $t = \ln(k/\Lambda)$. The effective average action Γ_k interpolates between a microscopic or bare UV action $S_\Lambda = \Gamma_{k\to\Lambda}$ and the full quantum effective action $\Gamma = \Gamma_{k\to0}$ in the infrared and governs the dynamics of the field expectation values after the integration of quantum fluctuations from the UV scale Λ down to the infrared scale k_{IR}. The infrared regulator R_k specifies the regularization of quantum fluctuations near an infrared momentum shell with momentum k and $\Gamma_k^{(2)}$ denotes the second functional derivative of the effective average action with respect to the fields of the given theory. The trace represents a summation and integration over all discrete and continuous indices. The highly nonlinear Wetterich equation has a simple one-loop structure but includes higher loop contributions in perturbation theory since the full nonperturbative propagator enters the loop diagram. One advantage of this approach is that it does not rely on the existence of a small expansion parameter and thus is applicable in the nonperturbative regime. QCD-related reviews on the functional RG approach can be found in [39].

In order to solve the functional equation numerically some truncations are required that turn it into a finite-dimensional partial differential equation. This truncation might induce a certain dependence of physical observables on the regulator, but this can be minimized by choosing optimized regulators or by implementation of RG consistency [40]. In this work, a modified three-dimensional flat regulator has been used [41].

The flow equation for Γ_k must be supplemented with an initial condition at $k = \Lambda$ which according to Eq. (4) reads for three flavors

$$
\Gamma_{k=\Lambda} = \int d^4x \bar{q}(\partial\!\!\!/ + gT_a(\sigma_a + i\gamma_5\pi_a))q + \mathrm{Tr}(\partial_\mu\Phi^\dagger\partial_\mu\Phi) + \Omega_{k=\Lambda}^{(2+1)}(\rho_1, \tilde{\rho}_2) \quad (20)
$$

with $\tilde{\rho}_2 := \rho_2 - \rho_1^2/3$. This truncation for the effective action corresponds to a leading-order derivative expansion with standard kinetic terms for the meson fields. Note that in this local potential approximation (LPA) no scalar wave function renormalizations and no scale-dependence in the Yukawa couplings between quarks and mesons are taken into account. However, in this truncation the important dynamical backreaction of the mesons on the quark sector of the model is already included. For more details see [36].

Finally, this yields for three quark flavors the IR and UV finite flow equation for the effective potential

$$
\frac{\partial\Omega_k^{(2+1)}}{\partial k} = \frac{k^4}{12\pi^2}\left\{\sum_b \frac{1}{E_b}\coth\left(\frac{E_b}{2T}\right) - 2N_c\sum_{f=u,d,s}\frac{1}{E_f} \right.
$$
$$
\left. \times\left[\tanh\left(\frac{E_f - \mu_f}{2T}\right) + \tanh\left(\frac{E_f + \mu_f}{2T}\right)\right]\right\}, \quad (21)
$$

where now the flow of the mesonic degrees of freedom is taken into account. The meson energies $E_b = \sqrt{k^2 + m_b^2}$ include the RG scale dependent meson masses m_b which are obtained by diagonalizing the mass entries of the matrix

$$
M_{k,ab}^2 := \frac{\partial^2\Omega_k}{\partial\phi_a\partial\phi_b}. \quad (22)
$$

Details and the lengthy explicit expressions of the eigenvalues can be found in [36]. Evolving the system toward the infrared yields the full thermodynamic potential evaluated at the solution of the gap equation, i.e., the minimum of the grand potential.

As initial UV condition for the flow Eq. (21) the meson potential is parametrized as

$$
\Omega_{k=\Lambda}^{(2+1)} = U_{\chi,k=\Lambda}(\rho_1, \tilde{\rho}_2) - c_A\xi - c_l\sigma_l - c_s\sigma_s \quad (23)
$$

with the scale-dependent chiral potential

$$
U_{\chi,k=\Lambda}(\rho_1, \tilde{\rho}_2) = a_{10}\rho_1 + \frac{a_{20}}{2}\rho_1^2 + a_{01}\tilde{\rho}_2 \quad (24)
$$

which differs only in the second argument $\tilde{\rho}_2$ from the corresponding chiral potential in mean-field approximation Eq. (15). Note that only the expansion coefficients a_{ij} in the potential are scale dependent while all remaining parameters are kept constant. See Appendix A for the initial parameter fixing.

For two quark flavors the flow, Eq. (21), simplifies to

$$
\frac{\partial\Omega_k^{(2)}}{\partial k} = \frac{k^4}{12\pi^2}\left\{\frac{1}{E_\sigma}\coth\left(\frac{E_\sigma}{2T}\right) + \frac{3}{E_\pi}\coth\left(\frac{E_\pi}{2T}\right) \right.
$$
$$
\left. - \frac{2N_c}{E_q}\sum_{f=u,d}\left[\tanh\left(\frac{E_q - \mu_f}{2T}\right) + \tanh\left(\frac{E_q + \mu_f}{2T}\right)\right]\right\},
$$
$$
(25)
$$

with only one scalar σ and three pion degrees of freedom.

Moreover, for $T = 0$ and N_f generic quark flavors the flow reduces to

$$
\left.\frac{\partial\Omega_k}{\partial k}\right|_{T=0} = \frac{k^4}{12\pi^2}\left[\sum_b\frac{1}{E_b} - 4N_c\sum_f\frac{1}{E_f}\theta(E_f - \mu_f)\right]. \quad (26)
$$

In this limit the Fermi-Dirac distributions of the fermionic threshold functions in Eq. (21) or in Eq. (25) become a sharp Heaviside function. Hence, for $\mu_f^2 > m_f^2$, only scales above the Fermi sea $k^2 > k_{f,\mathrm{sea}}^2$ with $k_{f,\mathrm{sea}}^2 \equiv \mu_f^2 - m_f^2$ contribute to the corresponding quark loop and are integrated out yielding a finite quark density. Hence, increasing the chemical potential suppresses more and more the quark dynamics of the model. The μ_f independence below the onset chemical potential for the density is related to the so-called "Silver Blaze property" [42]. In the following we will refer to this phenomenon in that manner.

Note that at vanishing temperature the quark-meson model is equivalent to its Polyakov-loop extended version, the Polyakov-quark-meson (PQM) model [43]. In such PQM models the deconfinement phase transition is captured statistically by including an effective potential for the gluon background field in terms of the order parameter fields for deconfinement, the Polyakov loops. There are basically two major modifications by the Polyakov loops which vanish in the zero temperature limit exactly: all known variants of the effective Polyakov loop potential [44–47] are proportional to the temperature and the implicit dependence of the Polyakov-loop variables on the quark loop dynamics degenerate to a standard Fermi-Dirac distribution without a Polyakov-loop contribution. Hence, exactly at $T = 0$ the Polyakov-loop in this context is irrelevant for the thermodynamics at $\mu > 0$. However, a phenomenological finite density generalization of the Polyakov loop potential at zero temperature can stiffen the

EoS [48]. For a recent review see, e.g., [49] and for recent (P)QM phase structure investigations with the FRG see e.g., [50].

III. PHASE STRUCTURE

The bulk thermodynamics of the system is determined by the effective potential which depends in the case of two flavors on one (nonstrange) condensate and for three or, more precisely, $(2 + 1)$ flavors on two (one nonstrange and one strange) condensates. The condensates are determined by minimizing the total effective potential with respect to the corresponding fields, here generically denoted by Φ,

$$\left. \frac{\partial \Omega}{\partial \Phi} \right|_{\Phi = \langle \Phi \rangle} = 0. \tag{27}$$

This yields the chiral nonstrange σ_l and strange σ_s condensates or expectation values as functions of the external parameters, i.e., the temperature and the quark chemical potentials. The thermodynamic pressure is just the negative of the effective potential evaluated at the minimum and normalized in vacuum

$$p = -(\Omega - \Omega^0)|_{\Phi = \langle \Phi \rangle}. \tag{28}$$

In the FRG case, the infrared-evolved potential $\Omega_{k=0} - \Omega^0_{k=0}$ has to be used.

By varying the external parameters the phase structure of the chiral transition can now be analyzed. For simplicity, we consider here a common chemical potential for all quark flavors, i.e., we set $\mu_e = 0$ in Eq. (11). Our numerical findings are collected in Fig. 1 where the phase diagrams for two quark flavors (dotted/solid lines) and for three
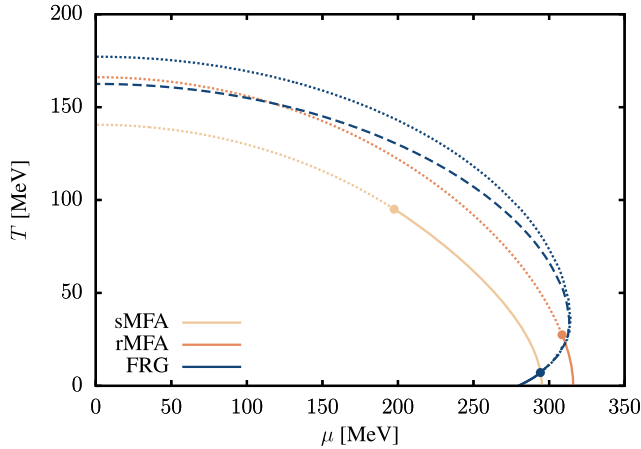

FIG. 1. Phase diagrams of the $N_f = 2$ quark-meson model in three different approximations (sMFA, rMFA, and FRG). The dots are critical endpoints. Dotted lines are smooth crossovers and solid lines first-order phase transitions. In addition, the corresponding $N_f = 2 + 1$ flavor phase structure obtained with the FRG is also shown (dashed line).

flavors (dashed line) are shown. The numerical input parameters and contingent cutoff dependency are collected in Appendix A; details on the numerical implementation can be found in Appendix B.

Typical for the phase structure obtained with the FRG is the back-bending behavior of the chiral phase transition line (blue lines) for small temperatures characterized by a positive slope of the critical chemical potential as a function of temperature. The critical endpoints (CEPs) are denoted as dots in the figure and the crossover regions/first-order transitions as dotted and solid lines, respectively. The origin of this back-bending phenomenon is not yet completely clarified. It might be related to the fact that additional interaction channels should be considered, see [51] for a detailed discussion. For the chosen vacuum input parameters and in the LPA truncation of the FRG equation, see Appendix A, the CEP is located at very small temperatures, around $T \sim 10$ MeV for two and three quark flavors. In mean-field approximations the thermodynamical behavior at small temperatures is different and the first-order transition line hits the chemical potential axis perpendicularly [51].

Furthermore, since the inclusion of fluctuations generically smoothes the chiral phase transition, the crossover transition line is shifted to higher temperatures if more fluctuations in the thermodynamic potential are taken into account [50], except at very low temperatures where the back-bending phenomenon takes over. This is nicely demonstrated in Fig. 2(a) where both the light (solid lines) and the strange (dashed lines) chiral condensates are shown as a function of temperature for vanishing quark chemical potential.

In sMFA where only the thermal quark loop contribution is considered, the pseudocritical crossover temperature $T_c \approx 140$ MeV at $\mu = 0$ is smallest. Already the inclusion of the vacuum quantum fluctuations of the quarks, labeled as rMFA in the figures, lifts the pseudocritical temperature by about 30 MeV. Interestingly, the whole chiral phase transition is shifted constantly toward higher temperatures by roughly this amount for all chemical potentials, cf. Fig. 1. As a consequence, the first-order transition at $T = 0$ is also pushed to higher chemical potentials as visible in Fig. 2(b). This trend is continued at least for moderate chemical potentials when additionally meson fluctuations with the FRG are taken into account. However, for smaller temperatures and due to the back-bending of the transition line, see. Fig. 1, the critical chemical potential is pushed to smaller values in contrast to the previous argument. This will later be of relevance for the EoS.

All condensates exhibit for $T = 0$ a first-order phase transition close to $\mu \approx 300$ MeV corresponding to the light quark mass in the vacuum. In sMFA, the first-order transition is strongest, in FRG weakest. Hence, the gap in the FRG light condensate is quite small and melts only moderately after the transition, still signaling a chirally
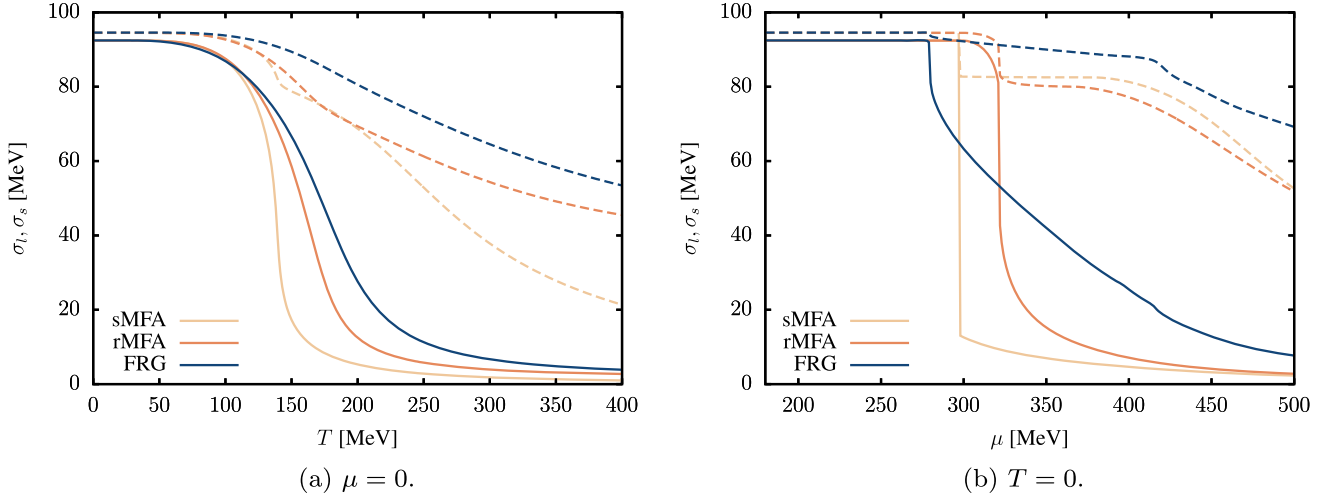
FIG. 2. Chiral condensates in the $N_f = 2 + 1$ flavor quark-meson model in three different approximations (FRG, rMFA and sMFA). The light condensates σ_l (solid) are the lower lines and the strange condensates σ_s (dashed) the upper lines.

broken phase in this density regime of the phase diagram [52]. In rMFA the light condensate is constant until $\mu = 300$ MeV and melts down before the first-order jump which is consistent with the Silver Blaze property. It is likely that for a sigma mass below 560 MeV the rMFA condensates immediately jump at the light quark masses as well.

Just below a quark chemical potential of about 430 MeV, the value that coincides with the strange quark mass in the vacuum, a further decrease is seen in all three strange condensates and a smooth chiral phase transition takes place.

However, when strange quarks are added to the system an opposite behavior is found for vanishing and moderate chemical potentials and the three-flavor crossover line is pushed down again, see the dashed line in Fig. 1. The difference to the two-flavor phase structure shrinks for decreasing temperatures. Below $T < 50$ MeV almost no influence of the strange quark on the transition line is observed where the dashed line merges with the solid two-quark flavor line.

IV. EOS FOR QUARK AND HYBRID STARS

The equations of state (EoS) for symmetric quark matter, i.e., for equal chemical potentials, obtained in MFAs and with the FRG, are compared to each other in Fig. 3(a). Solid lines are the two-quark flavor findings and the dashed lines the corresponding three-flavor calculations. The numerical results are almost insensitive to the strange quark before the onset of the strange chiral phase transition around energy densities $\varepsilon \approx 550$ MeV/fm^3 but start to deviate thereafter, see Fig. 3(a). In MFAs the transition is more gradually
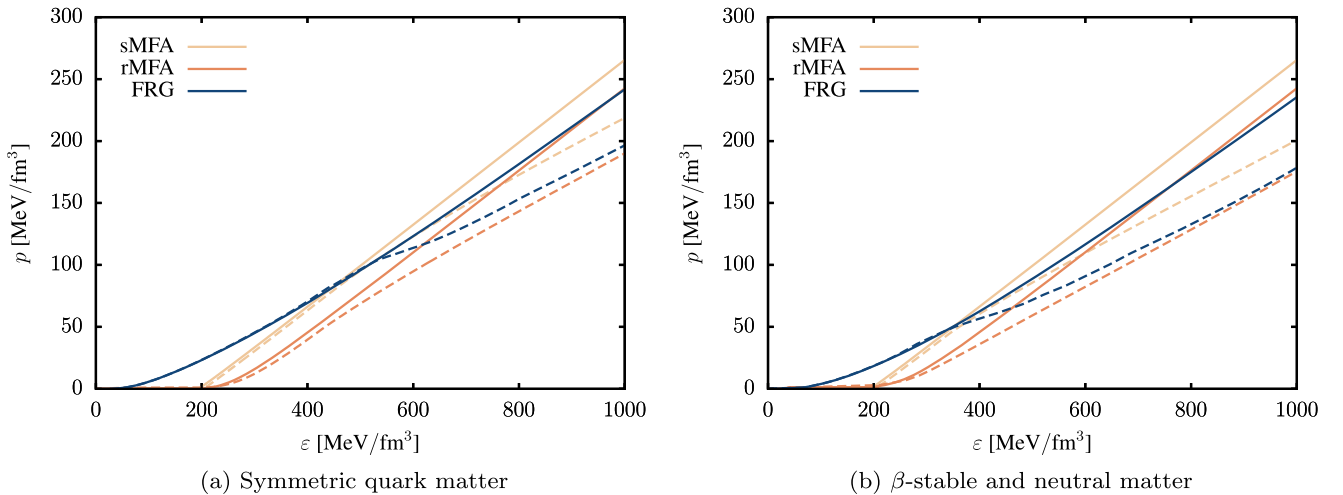

FIG. 3. Three different EoS of the $N_f = 2$ (solid) and $N_f = 2 + 1$ (dashed) quark-meson model at $T = 0$ for $m_l \approx 300$ MeV, $m_s \approx 430$ MeV and $m_\sigma = 560$ MeV.

realized and the deviation is less pronounced than within the FRG. This can already be seen in Fig. 2(b) where the strange condensate in MFA decreases moderately for chemical potentials smaller than the strange quark mass $m_s \approx 430$ MeV. In the FRG curve there is a more rapid onset with a steeper slope around the strange quark mass. Note that this behavior could also be related to a second phase transition in the light quark sector as has been found in [52].

Furthermore, it is obvious that vacuum fluctuations reduce the slope of the EoS, i.e., the sound speed, and over most of the shown density range the EoS obtained in FRG has still a smaller slope, see Sec. IV A.

With the inclusion of a free relativistic electron gas and the conditions for weak equilibrium and charge neutrality, cf. Eqs. (11) and (12), we obtain slightly modified EoS. The results for β-stable and neutral matter are presented in Fig. 3(b). Differences to the result for symmetric quark matter are visible almost exclusively for $N_f = 2 + 1$ where the weak equilibrium and charge neutrality conditions render the population of strange quarks more favorable. Hence, the onset of strangeness is pushed to smaller energy densities, leading to a pressure reduction for a given energy density beyond the onset.

Note that in charge neutral and β-equilibrated matter isospin symmetry is broken and the chemical potentials of the *up* and *down* quarks split. However, our approximation with only one chiral light condensate σ_l for both *up* and *down* quark flavors yields in all cases degenerated *up*- and *down*-quark masses. For large μ the restoration of chiral symmetry in the light quark sector suppresses both quark masses such that only small mass differences are expected there in contrast to the behavior in the vicinity of the chiral transition. The impact on the EoS might be more pronounced, and the small difference between symmetric and charge neutral matter in the two-flavor case might be an artefact of this approximation. For a more complete analysis including isospin symmetry breaking the introduction of an additional third chiral condensate is necessary which is, however, beyond the scope of the present work.

In order to allow for a description of hybrid stars with a phase transition from hadronic to quark matter in the interior of the star we combine the quark matter EoS with a nuclear one. The transition is achieved with a standard Maxwell construction[1] that maximizes the pressure for a given chemical potential. For the nuclear EoS we consider some representative models compatible with several nuclear physics constraints as well as the maximum neutron star mass and the GW170817 tidal deformability. Three of them are energy density functional models, one is based on a nonrelativistic Skyrme parameterization, RG(SLy4) [54],

---

[1]This assumes a high surface tension at the hadron-quark interface, see e.g., [53] for a discussion of this point in the context of a potential hadron-quark transition within hybrid stars.
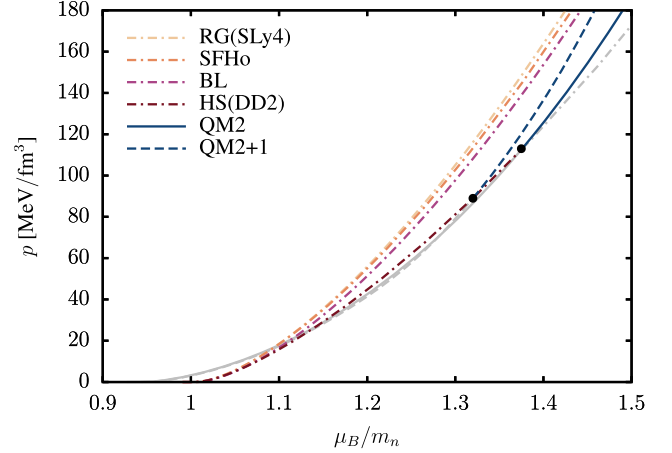

FIG. 4.   Pressure as a function of the baryon chemical potential in units of the neutron mass for various hadronic RMF models (dash-dotted) compared to the $N_f = 2$ (solid) and $N_f = 2 + 1$ (dashed) QM EoS in FRG (β-equilibrated and neutral quark matter). Intersections (black dots) of the quark-matter pressure with the HS(DD2) model at higher pressure are found while (unphysical) intersections at lower pressure are ignored, see text for details.

and two are relativistic mean field models, HS(DD2) [55] and SFHo [56]. The BL EoS [57] is formulated in the framework of the Brueckner-Bethe-Goldstone many-body theory with chiral nuclear forces.

In Fig. 4 a comparison of different nuclear EoS (dash-dotted lines) with the $N_f = 2$ (solid) and $N_f = 2 + 1$ (dashed) EoSs evaluated with the FRG respecting β-equilibrium and charge neutrality is given. We do not consider the FRG results as very realistic at low densities below $\mu_B/m_n \lesssim 1.2$, where a hadronic phase is expected. In addition, the attractive meson interactions in the QM model, lead to a very high pressure for a given chemical potential in this range. We only present it for completeness. Disregarding the unphysical part of the QM EoS obviously all nuclear EoS except the HS(DD2) EoS produce higher pressure than the QM one at a given baryon chemical potential ($\mu_B = 3\mu$) for the entire range of interest for compact stars. Hence, no hybrid stars could exist with these model combinations. The pressure of the HS(DD2) EoS intersects the two-flavor FRG pressure curve around $\mu_B/m_n \approx 1.38$ corresponding to the appropriate physical transition from nuclear to quark matter.

By construction, the combination of the two-flavor QM EoS from the FRG with the HS(DD2) EoS leads to a first-order phase transition between the confined nuclear matter and the deconfined quark matter which is characterized by a discontinuity in the energy density. This can be observed in Fig. 5 which depicts the constructed hybrid $N_f = 2$ (DD2 + QM2) and $N_f = 2 + 1$ (DD2 + QM2 + 1) EoSs in comparison to the hybrid EoS QHC19 [58] and a
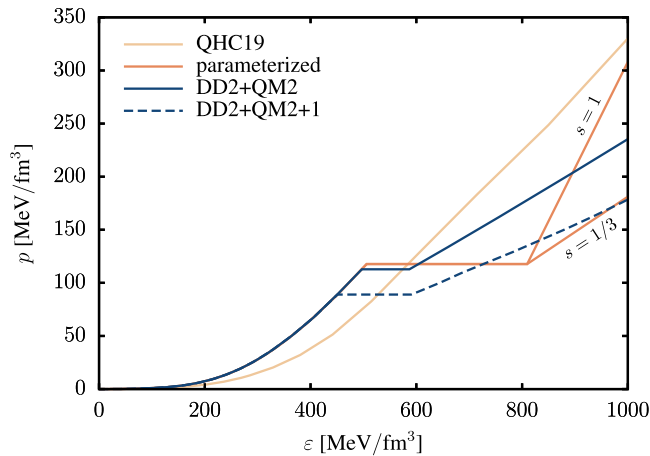
FIG. 5.   Composite EoS for the QM and DD2 nuclear model, cf. Fig. 4, compared with the hadron quark EoS QHC19 [58] and a combination of the HS(DD2) EoS with a parametrized quark matter EoS [59] for $c_s^2 \equiv s = 1$ or $1/3$, respectively. While the QHC19 model features a continuous quark-hadron transition, the others employ a Maxwell-constructed first-order transition and a discontinuity in the energy density ε.

parametrized EoS [59].[2] The QHC19 EoS features a smooth crossover quark-hadron transition. For the parametrized EoS the HS(DD2) EoS is used for the hadronic regime and the quark matter side is parametrized as

$$p(\varepsilon) = \begin{cases} p_c, & \varepsilon_c < \varepsilon < \varepsilon_c + \Delta\varepsilon \\ p_c + s[\varepsilon - (\varepsilon_c + \Delta\varepsilon)], & \varepsilon > \varepsilon_c + \Delta\varepsilon, \end{cases}$$

(29)

which describes a first-order transition at $\{\varepsilon_c, p_c\}$ with energy gap $\Delta\varepsilon$ and a constant slope $s = \partial p/\partial\varepsilon$, i.e., a constant quark matter sound speed squared, thereafter. Following the idea of Ref. [59], we choose $p_c = 1.89 \times 10^{35}$ dyn cm^{-2} and $\varepsilon_c = 9.02 \times 10^{14}$ g cm^{-3} which corresponds to $n_c \approx 3n_0$ and $\Delta\varepsilon/\varepsilon_c = 0.6$. For the slope, we consider two extreme parameterizations, one with $s = 1/3$ corresponding to the asymptotical QCD value, and one with $s = 1$ corresponding to the maximally allowed sound speed by causality. This ensures the onset of the phase transition at similar densities to those found in our hybrid construction with two-flavor QM. The large gap in the energy density has been chosen to produce twin stars, i.e., an additional branch of hybrid stars with the same mass but different radius than their nuclear counterpart [61]. Such twin star configurations are found, for example, in studies with NJL quark matter including additional repulsive 8-quark interactions [62]. A comparison of that

---

[2]Note that all employed nuclear EoSs, the QHC19 EoS as well as our hybrid star EoSs with the FRG are available online in the CompStar Online Supernovae Equations of State (CompOSE) database [60], see https://compose.obspm.fr/.

parameterization to the FRG calculation in Fig. 5 reveals that the energy gaps in our construction are much too small to produce a disconnected second branch but favor a single connected hybrid-nuclear branch. In fact, our two-flavor hybrid model is well reproduced by values of $\Delta\varepsilon/\varepsilon_c = 0.18$ and $p_c/\varepsilon_c = 0.23$ and a constant $c_s^2 = 1/3$ on the quark matter side. These values lie well in between the region identified in [61] as that giving rise to a connected branch. Similar arguments show that the hybrid model with $2 + 1$ flavors on the quark side again leads to a connected branch.

A. Sound speed

More information on dense matter can be gained through a detailed investigation of the speed of sound [63]. It measures the stiffness of the EoS for a one fluid flow by the thermodynamic derivative of the pressure with respect to the energy density at constant entropy and particle numbers

$$c_s^2 \equiv \left. \frac{\partial p(\varepsilon)}{\partial\varepsilon} \right|_{S,N_i}$$

(30)

and can be identified as the speed of propagation of sound waves. Causality implies an upper bound $c_s^2 \leq 1$ and thermodynamic stability a lower bound $c_s^2 > 0$. For an ideal gas composed of pointlike ultrarelativistic (massless) components the squared speed of sound is equal to one third, $c_s^2 = 1/3$. This is common to all systems with conformal symmetry of which an ideal massless gas is just an example. Even for any strongly interacting system the vanishing of the trace of the energy-momentum tensor, a feature of conformal theories, implies that the energy density is connected to the pressure by $\varepsilon = 3p$ hence yielding $c_s^2 = 1/3$ independently of density, temperature, or interactions. The speed of sound is decreased such that $c_s^2 < 1/3$ when a mass for the components is included or when (perturbative) interactions among the components take place. In the case of QCD at asymptotically high densities or temperatures, far exceeding the densities in the core of compact stars, a weak coupling expansion is valid (pQCD) such that c_s^2 is expected to reach the conformal limit with increasing density from below [64]. This behavior is confirmed in QCD lattice calculations at finite temperature as well as at zero and small baryon chemical potentials [65].

The speed of sound has also been investigated in alternative theories for which for example the AdS/CFT correspondence holds where calculations in the strong coupling limit are feasible, see, e.g., [66]. It has been conjectured that c_s^2 is always bounded from above in such classes of strongly coupled field theories by the conformal value of $1/3$ [67] although recently counterexamples have been presented [68]. For more details of this conjecture see [64].
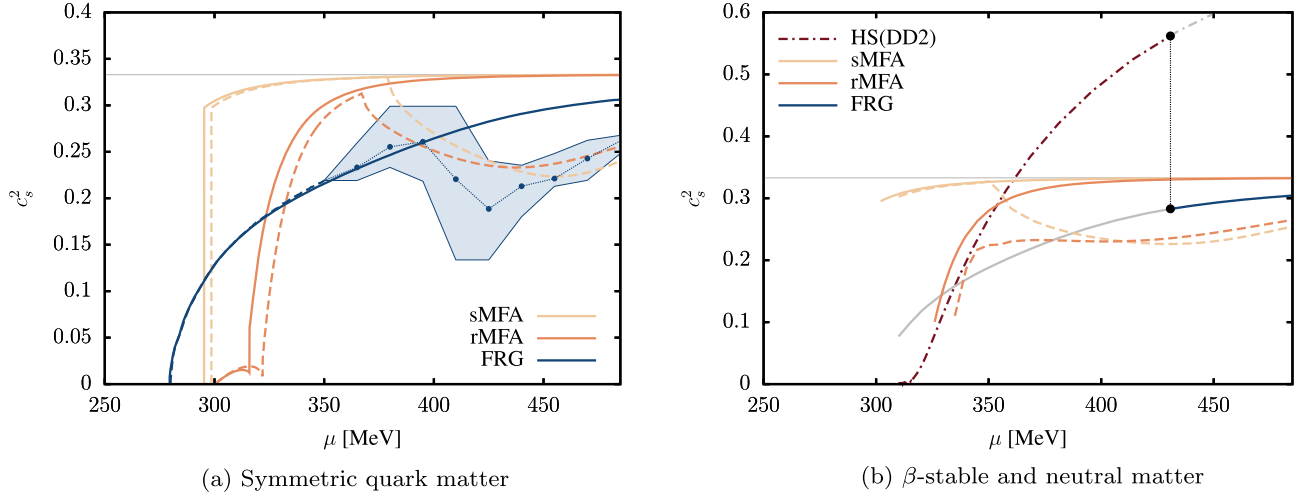
(a) Symmetric quark matter

(b) β-stable and neutral matter

FIG. 6.   Sound speed squared c_s^2 at zero temperature as a function of μ for three different quark matter EoS and the hadronic DD2 EoS (solid $N_f = 2$, dashed $N_f = 2 + 1$; left panel: flavor symmetric matter, right panel: β-equilibrated neutral matter). The thin horizontal lines indicate the Stefan-Boltzmann limit $c_s^2 = 1/3$. The vertical black-dotted line in the right panel illustrates the first-order transition from the hadronic HS(DD2) to the QM2 EoS, cf. Fig. 5. The metastable phases are extrapolated in gray color. For the blue error in the left panel band see Appendix B.

The speed of sound of the QM model in both mean-field approximations and the FRG calculation is found generally to be always smaller than $c_s^2 = 1/3$. An alternative scenario could be the presence of a bump in c_s^2 at intermediate densities before approaching the upper bound from below asymptotically and thus implying the existence of a maximum and a local minimum of c_s^2 as a function of the chemical potential. This scenario is supported by another recent FRG analysis including diquark condensation [29] where a maximum in c_s^2 above $1/3$ is found. The additional inclusion of vector interactions in the quark-meson model [69] is also expected to stiffen the EoS.

Our result for the speed of sound of quark matter with a flavor-symmetric chemical potential is shown in Fig. 6(a). In the $N_f = 2$ mean-field approximation (solid lines) the speed of sound converges to the limit $c_s^2 = 1/3$ while the addition of strange quarks (dashed lines) leads to a reduction of c_s^2 around scales of the strange chiral phase transition. This behavior has already been observed in Fig. 3(a) and is expected due to the additionally populated strange quark states softening the EoS. In the FRG solution, the speed of sound is generally smaller than the asymptotic mean-field values beyond the transition which can be attributed to the quantum fluctuations captured within the FRG approach.

Furthermore, the strength of the first-order chiral phase transition, i.e., the gap in the order parameter, is found to correlate with the size of the jump in the speed of sound. Hence, the strong first-order transition in sMFA leads to a jump of c_s^2 close to its asymptotic Stefan-Boltzmann value $c_s^2 = 1/3$ which leads to the almost linear behavior of the EoS even at low pressure, see Fig. 3(a). The more washed-out transition in rMFA induces an initially smaller slope of

the EoS. This becomes more significant in the FRG calculation: due to an even smoother transition a comparably small gap $\Delta\varepsilon$ is found in Fig. 3(a). In agreement with Fig. 6(a) the slope is consistently smaller than that of the mean-field calculations.

For $N_f = 2 + 1$, c_s^2 is found to be sensitive to the numerical error caused by the employed solution method of the flow equation which leads to visible fluctuations at high μ. Therefore, Fig. 6(a) depicts for $\mu > 350$ MeV averaged values in conjunction with error intervals displayed as blue band. For more technical details see Appendix B.

The speed of sound for β-stable and charge-neutral quark matter is displayed in Fig. 6(b). Note that due to the usage of only one light condensate, the first-order transition cannot be resolved exactly in this approximation and hence the drop of the speed of sound to zero at low chemical potential is not shown. Due to the numerical uncertainties mentioned above, we postpone a careful $N_f = 2 + 1$ analysis to a future work. Qualitatively, we observe the same behavior as for a flavor-symmetric chemical potential. However, in mean-field approximation we find that the reduction of the speed of sound due to the onset of strangeness takes place at lower chemical potentials and more gradually than in symmetric quark matter. This is in agreement with the onset of strangeness already at small energy density, see Fig. 3(b) and the discussion in the previous section. In Fig. 6(b) we also show the speed of sound for the HS(DD2) nuclear EoS and indicate the transition point to quark matter in the DD2 + QM2 EoS by a vertical line. As suggested in [70], this discontinuity in the speed of sound can be related to a δ-function singularity in the fundamental derivative, leading to possibly non-convex thermodynamics.

(a) Pure quark stars

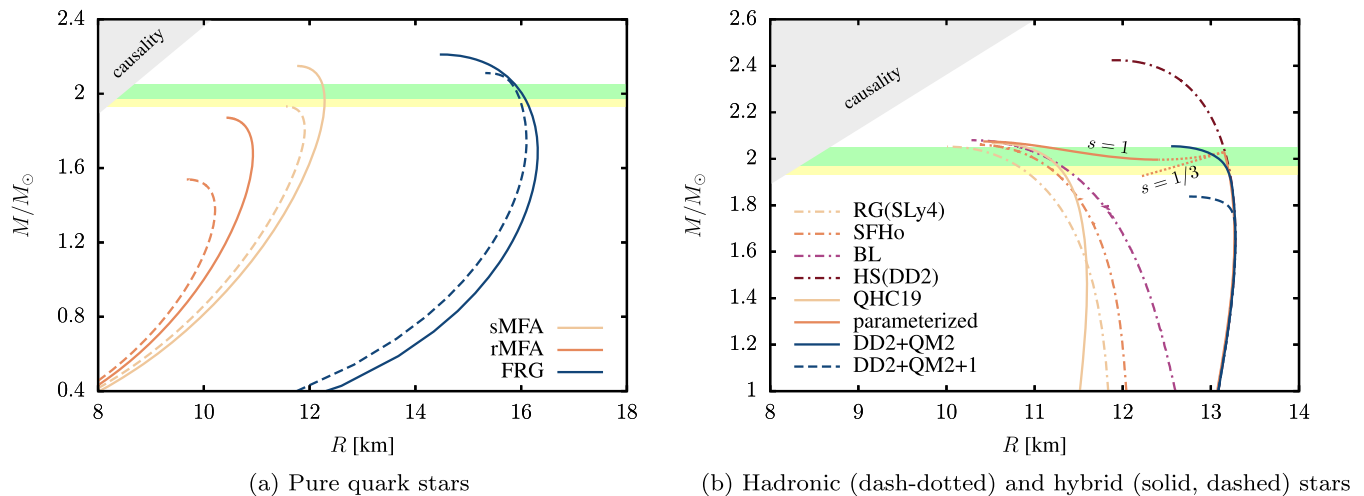(b) Hadronic (dash-dotted) and hybrid (solid, dashed) stars

FIG. 7. Neutron star mass-radius relations for β-equilibrated and neutral matter. Left: pure quark stars for $N_f = 2$ (solid) and $N_f = 2 + 1$ (dashed). Right: purely hadronic stars (dash-dotted) obtained from various nuclear model EoS, cf. Figs. 4 and 5. Hybrid stars from the combined HS(DD2) model with the FRG solutions for QM (solid, dashed). Horizontal bands: PSR J1614 − 2230 (yellow) and PSR J0348 + 0432 (green) mass measurements [1]. See text for details.

B. Neutron star models

In order to determine the influence of fluctuations on the mass-radius relation of a neutron star, we employ hydrostatic equilibrium solutions for a relativistic spherically symmetric compact star composed of a perfect fluid, which have been derived from Einstein's equations by Tolman, Oppenheimer and Volkoff (TOV) [71]. In Schwarzschild coordinates the corresponding equations determining the pressure p and the enclosed gravitational mass M of the star as a function of the radius r read[3]

$$\frac{dp(r)}{dr} = -\frac{G}{r}\frac{[p(r) + \varepsilon(r)][M(r) + 4\pi r^3 p(r)]}{(r - 2GM(r))} \quad (31)$$

$$\frac{dM(r)}{dr} = 4\pi r^2 \varepsilon(r), \quad (32)$$

wherein ε denotes the energy density and G the gravitational constant. For a given EoS in terms of $p(\varepsilon)$ as input these equations can be integrated from the origin for a given choice of a central pressure p_0, i.e., $p(r = 0) = p_0$ and $M(r = 0) = 0$. The value of the radius where the pressure vanishes, i.e., $p(r = R) = 0$, defines the surface and thus the gravitational mass $M(R)$ and radius R of the star. Varying the unknown central pressure p_0 yields the mass-radius relation.

The mass-radius relations for the pure β-stable and charge-neutral quark matter EoS are shown in Fig. 7(a) for three different approximations. Please keep in mind that quark matter is not absolutely stable within our setup and that thus such pure quark stars could not exist. We,

---

[3]In this work we employ natural units $c = \hbar = 1$.

nevertheless, show the mass-radius relations, since they are instructive to understand the impact of the fluctuations. Solid lines are the solutions for a two-flavor EoS and dashed lines the three-flavor results. In general, all three-flavor calculations yield a smaller maximum mass than the corresponding two-flavor results, which can be understood by the softening of the EoS due to the additional strange degrees of freedom. Only the two-flavor sMFA and both the two- and three-flavor FRG results yield a maximum mass above $2\,M_\odot$. Furthermore, the inclusion of the renormalized vacuum fluctuations in the rMFA in contrast to the sMFA leads to smaller masses and radii. The additional consideration of mesonic fluctuations via the full FRG computation increases the maximum mass even slightly beyond the sMFA result but also leads to significantly larger radii. The reason is that within the present FRG setup, the density jump at the surface is much smaller than in the MFA calculations, see Fig. 3(b), such that the star becomes much less compact and can accumulate more mass. For the sake of completeness the causality constraint $R \leq 2.87GM$ [4] is also displayed in the figure.

The mass-radius relations from the combined EoSs for a hybrid star with the $N_f = 2$ or $N_f = 2 + 1$ quark-meson matter side employing the FRG, respectively, and a hadronic phase parametrized by the HS(DD2) EoS are presented in Fig. 7(b), labeled again as DD2 + QM2 and DD2 + QM2 + 1. For $N_f = 2$, the onset of quark matter leads to the visible separation of the DD2 and the DD2 + QM2 curve slightly below $M = 2\,M_\odot$ corresponding to a central baryon number density of approximately 0.47 fm^{-3}. Below this value, the hybrid star mass-radius-relation coincides with the nuclear HS(DD2) one as it should. For $N_f = 2 + 1$, the DD2 + QM2 + 1 curve exhibits a similar behavior, but the onset of quark matter occurs at a

smaller baryon number density of approximately 0.43 fm^{-3}. Thus, since the transition occurs well above nuclear saturation density, both hybrid EoSs satisfy constraints from nuclear physics as implemented in the HS (DD2) EoS. The maximum hybrid star mass of about 2.1 $M_\odot$ for $N_f = 2$ complies well with current observations, whereas the $N_f = 2 + 1$ curve does not satisfy the 2 $M_\odot$ limit. Since the quark matter onset occurs only for masses slightly below 1.8 $M_\odot$ and higher, the value of the GW170817 tidal deformability obtained from both hybrid EoS does not change significantly with respect to the HS (DD2) value $\tilde{\Lambda} \approx 795$ for a mass ratio of 0.8 of the two coalescing stars. It is in slight tension with recent LIGO/ Virgo data [13,14] but in agreement with the observation that the HS(DD2) EoS leads to a relatively large radius for intermediate mass stars. The QHC19 model leads to a radius smaller by almost 2 km. For comparison, the *M*-*R* relations for four different pure nuclear RMF models (dash-dotted lines) are also shown in Fig. 7(b). As mentioned above, due to the small stiffness of the FRG quark matter EoS at high densities, a hybrid star construction with these nuclear EoS is not possible within the present setup.

As expected from Fig. 5, the parametrized EoS leads to a kink in the mass-radius relation at a mass slightly above the DD2 + QM2 curve. Contrary to the connected hadronic and hybrid branches in the latter, the large energy gap of the $s = 1$ parametrized EoS leads to a disconnected hybrid branch and therefore twin stars at masses of about 2 $M_\odot$. For $s = 1/3$, the pressure in the quark matter phase is not sufficient to counteract the strong gravitational pull due to the large energy density of the quark core, cf. Ref. [59], and thus does not support a stable hybrid star branch. Hence, we can rule out the occurrence of twin stars in our model due to the small energy gap at the phase transition from nuclear matter to quark matter and due to the small stiffness of the quark matter EoS. In case of a Maxwell construction with parameters that feature a larger energy gap, there might not even be any stable hybrid stars with a QM model quark matter description.

In summary we found that it is feasible to construct a hybrid nuclear-quark EoS where the quark matter part is obtained from an effective theory within the functional renormalization group approach. In particular, we would expect that the inclusion of repulsive interaction channels suspected to play a significant role might stiffen the quark matter EoS to a degree that allows for a realistic description of combined hadronic and quark matter with other hadronic models. Furthermore, it might deepen our understanding of the role and possible abundance of strange matter in compact stars.

V. SUMMARY AND CONCLUSIONS

The core of neutron stars contains strongly interacting matter at extreme densities, reaching several times nuclear matter saturation density for the most massive ones. Observations of neutron star properties, in particular precise high mass determinations [1] and the GW170817 tidal deformability [13,14], thereby put constraints on the equation of state for conditions not accessible to experiments. Although much recent progress has been achieved to pin down the EoS, many questions remain open, in particular on the composition of the inner core: does it contain non-nucleonic degrees of freedom? In addition to hyperons, nuclear resonances or mesons, a quark matter core might appear. In this paper we have performed a nonperturbative study of the quark matter EoS. We have considered a two- and three flavor quark-meson model, employing different approximations from mean-field to the functional renormalization group. Apart from including fluctuations in a nonperturbative way, the FRG has the potential power to generate the coupling parameters at low-energy scales from the underlying fundamental QCD at the UV, which would otherwise be just model parameters.

The quark-meson model fully incorporates chiral symmetry breaking and we have performed a first study of the impact of quantum and density fluctuations on the EoS for vanishing temperature. Since the different approximations of the grand potential were fixed to the same input parameters, our numerical findings are solely attributed to the impact of the fluctuations. As anticipated from studies of the phase diagram and confirmed by our investigations, fluctuations tend to smoothen the chiral phase transition, see, e.g., [36]. Within the EoS, the softening due to the appearance of strange quarks is therefore pushed to higher densities because the strange quarks are still heavier than the light quarks at higher densities. Quark stars obtained from the FRG, including fluctuations in the quark matter EoS, have higher maximum masses and radii compared with their mean-field counterparts. Furthermore, we have constructed a hybrid star EoS, combining our FRG quark matter EoS with a nuclear one via a Maxwell construction. The results for hybrid stars with a two-flavor quark matter core are in reasonable agreement with existing constraints. In contrast to many studies within the mean-field NJL model, see, e.g., [32], our FRG EoS allows for gravitationally stable hybrid stars with a three-flavor core, which however leads to a maximum mass below the highest observed pulsar masses. We notice that the inclusion of a repulsive vector interaction in the quark-meson model is expected to additionally stiffen the quark matter EoS and allow for constructing hybrid stars with nuclear EoS with smaller radii and tidal deformabilities.

We have presented here one of the first constructions of a nonperturbative EoS for high densities within the FRG that is a very promising nonperturbative method for computing the EoS directly from quark-gluon degrees of freedom, cf. [29,30]. Several approximations have been made, in particular:

(i) We have employed a quark-meson truncation of the effective action as a low-energy effective model for

QCD and solved the corresponding flow equation for the effective potential in lowest order of a derivative expansion. The quark-meson truncation comprises (pseudo-)scalar interaction channels which are the most dominant channels for chiral symmetry breaking at low temperatures and densities [72] but they might become insufficient at densities relevant for NSs such that in addition further channels like (axial-)vector ones should be taken into account.

(ii) For small temperatures and densities relevant for the NS interior dynamical baryonic correlations, i.e., the dynamical interrelation of three-quark states and baryonic degrees of freedom with confined quarks, become an increasingly important issue. This is obvious within the hadronic phase, where baryons and not quarks are the relevant degrees of freedom. Such correlations remain important at small temperatures within a deconfined phase, too. Within the FRG framework, the elaboration of the clustering of quarks into baryons as well as the emergence of long-range correlations between baryons is in principle straightforward. First successes could in parts already be achieved in a similar QCD related context [73]. This makes the QCD-based FRG approach toward lower densities very promising for future investigations. It should, however, be stressed that the computations becomes much more involved and much work is still necessary to technically cope with this issue.

(iii) Furthermore, the phase structure in this area of the QCD phase diagram is expected to be extremely rich with a wealth of possible different color superconducting phases [74,75]. Future work should address the inclusion of additional interaction channels like, for example, diquark-quark channels which allow for color superconductivity and the already mentioned repulsive (axial-)vector channels. Work along these lines is ongoing.

APPENDIX A: INPUT PARAMETERS

In this appendix the input parameters for the FRG and mean-field evaluations are summarized. In all $N_f = 2 + 1$ calculations we fix the axial $U(1)_A$ and chiral symmetry breaking parameters to $c_A = 4807.84$ MeV, $c_l = (120.73 \text{ MeV})^3$ and $c_s = (336.41 \text{ MeV})^3$ to reproduce the summed squares of the η and η' masses $m_\eta^2 + m_{\eta'}^2 = (1103.2 \text{ MeV})^2$, the pion mass $m_\pi = 138$ MeV, and the kaon mass $m_K = 496$ MeV, respectively, in the vacuum. With the three input parameters for the chiral potential, the sigma mass in the infrared has been set to $m_\sigma = 560$ MeV and the vacuum minima to $\sigma_{l,0} = 92.4$ MeV and $\sigma_{s,0} = 94.5$ MeV to yield the corresponding pion and kaon decay constants, $f_\pi = 92.4$ MeV and $f_K = 113$ MeV. With a Yukawa coupling of $g = 6.5$ the corresponding constituent quark masses are $m_l = g\sigma_{l,0}/2 \approx 300$ MeV and $m_s = g\sigma_{s,0}/\sqrt{2} \approx 434$ MeV. For $N_f = 2$, all strange quantities are omitted. g, c_l and the remaining two input parameters for the chiral potential are set to reproduce the subset m_l, m_π, m_σ and $\sigma_{k,0}$ in the same fashion as above.

The parameter set for the FRG and rMFA flow equations have been optimized by a global differential evolution algorithm [76] with an initial UV cutoff of $\Lambda = 1$ GeV. In the full FRG case we stopped the evolution around $k_{IR} = 80$ MeV where the condensates are already frozen and in the rMFA case we stop at $k_{IR} = 1$ MeV. Note that all obtained numerical results are insensitive to IR values when chosen in this region while a UV cutoff dependence for the rMFA results can still be seen. However, when choosing a UV cutoff larger than $\Lambda > 2$ GeV for the rMFA results any cutoff dependence disappears [77].

The used input parameters for the mean-field potentials can be found in Table I. The UV coefficients a_{ij} for the chiral potentials in the FRG calculations are listed in Table II. Further details on the input parameters can be found in Refs. [36].

TABLE I. Input parameters for the $N_f = 2$ and $N_f = 2 + 1$ quark-meson model for the sMFA and rMFA approximations. The Yukawa coupling is fixed at $g = 6.5$ and the sigma mass at $m_\sigma = 560$ MeV. For $N_f = 2 + 1$ flavor the $U(1)_A$-symmetry is explicitly broken by the parameter c_A.

N_f	Approximations	$m^2 [\text{MeV}^2]$	λ_1	λ_2
2	sMFA	$-(358.1)^2$	17.25	
2	rMFA	901.09^2	-5.38	
$2+1$	sMFA	384.71^2	-0.36	46.48
$2+1$	rMFA	1040.94^2	-2.65	11.73

TABLE II. FRG input parameters similar to Table I. Additionally, the utilized Yukawa coupling g and sigma mass m_σ are also quoted. The parameter a_{01} corresponds to the modified invariant $\tilde{\rho}_2$ by analogy with the mean-field parameter λ_2 in Table I.

N_f	g	$m_\sigma[\text{MeV}]$	$a_{10}[\text{MeV}^2]$	a_{20}	a_{01}
2	6.5	560	706.31^2	21.16	
$2+1$	6.5	560	515.70^2	37.45	47.68

APPENDIX B: NUMERICAL SOLUTION TECHNIQUES

The numerical methods employed for the solution of the FRG flow equations and for the TOV equations are outlined in this appendix.

The FRG flow equations (21) and (25) are partial differential equations (PDEs) including a partial derivative with respect to the RG scale k and field derivatives encoded in the mass terms. Several global as well as local solution schemes based on pseudo-spectral, finite volume, Taylor expansion or discontinuous Galerkin ideas are known, see [78] for some recent developments. Setting up a two-dimensional grid for the chiral potential in the variables

$$x = \sigma_l^2 \quad \text{and} \quad y = 2\sigma_s^2 - \sigma_l^2, \quad \text{(B1)}$$

cf. [36], and interpolating the derivatives from the discrete grid points, it is possible to reduce the PDE to a set of coupled ordinary differential equations (ODEs). For the interpolation, we use cubic splines in each of the two grid directions, respectively. The ODE solution is obtained from an explicit Runge-Kutta type step algorithm. For $N_f = 2$, the grid reduces to one dimension.

In the context of this work, the $T = 0$ limit of the flow equation, Eq. (26), is utilized wherein the fermionic threshold function reduces to a Heaviside function. This also encodes the Silver Blaze property of the theory because

$$E_l \geq m_l = g\sigma_{l,0}/2 \quad \text{(B2)}$$

implies that $\theta(E_f - \mu) = 1$ for all $\mu < m_f$ and hence the flow at the IR minimum $\sigma_{l,0}$ does not change with respect to the vacuum flow. Here we have assumed for simplicity a flavor-independent chemical potential. Of course, this property only holds for $\mu < \mu_c$ where μ_c signifies the chiral first-order transition. In both the sMFA and FRG solutions,

we observe $\mu_c < m_l$, cf. Fig. 2(b). Unfortunately, due to the utilized grid method the Silver Blaze property is subject to a numerical error. For any chemical potential, all grid points located at $\sigma_l < 2\mu/g$ display a different running than in vacuum. Since the bosonic energies incorporate field derivatives that are approximated from an interpolation of all grid points, the flow experiences small modifications at the IR minimum even if $\mu < m_l$. This effect aggravates when μ approaches m_l from below, $\mu \lesssim m_l$. It leads to fluctuations of the chiral condensate around the vacuum IR value. Those fluctuations are small and hardly visible in Fig. 2(b). However, they lead to an unphysical phase of very small but nonzero pressure. Furthermore, for a flavor-dependent chemical potential the first-order transition is additionally distorted by the error of our approximation, see Sec. IV. Thus, in the numerical treatment of the FRG EoS, data points close to the phase transition are omitted and the EoS from the physical phase with restored chiral symmetry is polynomially extrapolated down to $p = 0$. This procedure only affects the low-pressure outer region of the calculated pure quark stars. The dependence of the star radius on the extrapolation error has been checked and found to be negligible.

For $N_f = 2 + 1$, similar numerical fluctuations as discussed above are also found when μ_s approaches the order of the strange quark mass m_s at the current IR minimum. They are most prevalent in the determination of the speed of sound. A strong dependence of these fluctuations on the exact grid point configuration is observed and gives strong evidence for the claim as a numerical artifact. Therefore, in Fig. 6(a) for $\mu > 350$ MeV only the average derivative $\bar{c}_s^2 := \Delta p/\Delta\varepsilon$ is shown as dots, uniformly spaced at a distance of 15 MeV. For each dot, $\bar{c}_s^2$ has been calculated from the (p, ε) tuples at the dot to its left, itself, and the dot to its right. Furthermore, the highest deviation of the microscopically calculated, fluctuating speed of sound c_s^2 from $\bar{c}_s^2$ in the respective interval is indicated by the border points of the shaded region such that all c_s^2 data points lie within this region.

In the pure quark matter star calculations, the TOV equation is solved with an explicit Runge-Kutta algorithm. The evolution is stopped when the radial pressure $p(r)$ reaches a value of 10^{-5} relative to the central pressure. The EoS data points are interpolated with cubic splines, utilizing two separate splines in case of a discontinuity due to a first-order transition such as observed in the rMFA EoS.

[1] Z. Arzoumanian *et al.* (NANOGrav Collaboration), Astrophys. J. Suppl. Ser. **235**, 37 (2018); P. Demorest, T. Pennucci, S. Ransom, M. Roberts, and J. Hessels, Nature (London) **467**, 1081 (2010); J. Antoniadis *et al.*, Science **340**, 1233232 (2013).

[2] H. T. Cromartie *et al.*, Nat. Astron. **4**, 72 (2020).

[3] J. M. Lattimer and M. Prakash, Phys. Rep. **621**, 127 (2016).

[4] J. M. Lattimer and M. Prakash, Phys. Rep. **442**, 109 (2007).

[5] M. Oertel, M. Hempel, T. Klähn, and S. Typel, Rev. Mod. Phys. **89**, 015007 (2017).

[6] D. Chatterjee and I. Vidaña, Eur. Phys. J. A **52**, 29 (2016); H. Djapo, B.-J. Schaefer, and J. Wambach, Phys. Rev. C **81**, 035803 (2010).

[7] E. E. Kolomeitsev, K. A. Maslov, and D. N. Voskresensky, Nucl. Phys. **A961**, 106 (2017).

[8] M. Buballa *et al.*, J. Phys. G **41**, 123001 (2014); F. Weber, G. A. Contrera, M. G. Orsaria, W. Spinella, and O. Zubairi, Mod. Phys. Lett. A **29**, 1430022 (2014); M. Orsaria, H. Rodrigues, F. Weber, and G. A. Contrera, Phys. Rev. C **89**, 015806 (2014); A. Drago, A. Lavagno, and G. Pagliara, Phys. Rev. D **89**, 043014 (2014); M. G. Alford and S. Han, Eur. Phys. J. A **52**, 62 (2016).

[9] G. Baym, T. Hatsuda, T. Kojo, P. D. Powell, Y. Song, and T. Takatsuka, Rep. Prog. Phys. **81**, 056902 (2018).

[10] E. Witten, Phys. Rev. D **30**, 272 (1984); E. Farhi and R. Jaffe, Phys. Rev. D **30**, 2379 (1984).

[11] M. Buballa and M. Oertel, Phys. Lett. B **457**, 261 (1999); P. Haensel, J. Zdunik, and R. Schaeffer, Astron. Astrophys. **160**, 121 (1986), http://articles.adsabs.harvard.edu/pdf/1986A%26A...160..121H.

[12] A. L. Watts *et al.*, Rev. Mod. Phys. **88**, 021001 (2016).

[13] B. P. Abbott *et al.* (LIGO Scientific and Virgo Collaborations), Phys. Rev. Lett. **119**, 161101 (2017).

[14] B. P. Abbott *et al.* (LIGO Scientific and Virgo Collaborations), Phys. Rev. Lett. **121**, 161101 (2018).

[15] S. De, D. Finstad, J. M. Lattimer, D. A. Brown, E. Berger, and C. M. Biwer, Phys. Rev. Lett. **121**, 091102 (2018).

[16] E. R. Most, L. R. Weih, L. Rezzolla, and J. Schaffner-Bielich, Phys. Rev. Lett. **120**, 261103 (2018).

[17] C. D. Capano, I. Tews, S. M. Brown, B. Margalit, S. De, S. Kumar, D. A. Brown, B. Krishnan, and S. Reddy, Nat Astron. (2020), https://doi.org/10.1038/s41550-020-1014-6.

[18] J. S. Read, B. D. Lackey, B. J. Owen, and J. L. Friedman, Phys. Rev. D **79**, 124032 (2009); F. Özel, G. Baym, and T. Guver, Phys. Rev. D **82**, 101301 (2010); A. W. Steiner, J. M. Lattimer, and E. F. Brown, Astrophys. J. **765**, L5 (2013); J. Margueron, R. H. Casali, and F. Gulminelli, Phys. Rev. C **97**, 025805 (2018); I. Tews, J. Margueron, and S. Reddy, Phys. Rev. C **98**, 045804 (2018); E. Annala, T. Gorda, A. Kurkela, and A. Vuorinen, Phys. Rev. Lett. **120**, 172703 (2018).

[19] Y. Fujimoto, K. Fukushima, and K. Murase, Phys. Rev. D **98**, 023019 (2018).

[20] A. Kurkela, P. Romatschke, and A. Vuorinen, Phys. Rev. D **81**, 105021 (2010); J. F. Xu, G. X. Peng, F. Liu, D.-F. Hou, and L.-W. Chen, Phys. Rev. D **92**, 025025 (2015).

[21] O. G. Benvenuto and G. Lugones, Phys. Rev. D **51**, 1989 (1995); J. R. Torres and D. P. Menezes, Europhys. Lett. **101**, 42003 (2013).

[22] M. Baldo, M. Buballa, F. Burgio, F. Neumann, M. Oertel, and H. J. Schulze, Phys. Lett. B **562**, 153 (2003); M. Buballa, Phys. Rep. **407**, 205 (2005); R. C. Pereira, P. Costa, and C. Providência, Phys. Rev. D **94**, 094001 (2016); C.-M. Li, J.-L. Zhang, Y. Yan, Y.-F. Huang, and H.-S. Zong, Phys. Rev. D **97**, 103013 (2018).

[23] A. Zacchi and J. Schaffner-Bielich, Phys. Rev. D **100**, 123024 (2019); A. Zacchi, R. Stiele, and J. Schaffner-Bielich, Phys. Rev. D **92**, 045022 (2015).

[24] S.-S. Xu, Y. Yan, Z.-F. Cui, and H.-S. Zong, Int. J. Mod. Phys. A **30**, 1550217 (2015); T. Zhao, S.-S. Xu, Y. Yan, X.-L. Luo, X.-J. Liu, and H.-S. Zong, Phys. Rev. D **92**, 054012 (2015); P. Isserstedt, M. Buballa, C. S. Fischer, and P. J. Gunkel, Phys. Rev. D **100**, 074011 (2019); C. S. Fischer and J. Luecker, Phys. Lett. B **718**, 1036 (2013).

[25] T. Ishii, M. Järvinen, and G. Nijs, J. High Energy Phys. 07 (2019) 003.

[26] A. Peshier, B. Kampfer, and G. Soff, Phys. Rev. C **61**, 045203 (2000); Y.-L. Tian, Y. Yan, H. Li, X.-L. Luo, and H.-S. Zong, Phys. Rev. D **85**, 045009 (2012); T. Zhao, Y. Yan, X.-L. Luo, and H.-S. Zong, Phys. Rev. D **91**, 034018 (2015).

[27] S. Schramm, V. Dexheimer, and R. Negreiros, Eur. Phys. J. A **52**, 14 (2016).

[28] O. Hajizadeh and A. Maas, Proc. Sci., LATTICE2016 (**2016**) 358 [arXiv:1609.06979].

[29] M. Leonhardt, M. Pospiech, B. Schallmo, J. Braun, C. Drischler, K. Hebeler, and A. Schwenk, arXiv:1907.05814 [Phys. Rev. Lett. (to be published)].

[30] B. Friman and W. Weise, Phys. Rev. C **100**, 065807 (2019); M. Drews and W. Weise, Prog. Part. Nucl. Phys. **93**, 69 (2017); P. Pósfay, G. G. Barnaföldi, and A. Jakovác, Phys. Rev. C **97**, 025803 (2018).

[31] Z.-G. Dai, Q.-H. Peng, and T. Lu, Astrophys. J. **440**, 815 (1995).

[32] M. Buballa, F. Neumann, M. Oertel, and I. Shovkovy, Phys. Lett. B **595**, 36 (2004).

[33] A. Drago, A. Lavagno, and I. Parenti, Astrophys. J. **659**, 1519 (2007).

[34] D. Chatterjee, T. Elghozi, J. Novak, and M. Oertel, Mon. Not. R. Astron. Soc. **447**, 3785 (2015).

[35] W. Weise, Int. J. Mod. Phys. E **27**, 1840004 (2018).

[36] M. Mitter and B.-J. Schaefer, Phys. Rev. D **89**, 054027 (2014); B.-J. Schaefer and M. Wagner, Phys. Rev. D **79**, 014018 (2009).

[37] V. Skokov, B. Friman, E. Nakano, K. Redlich, and B.-J. Schaefer, Phys. Rev. D **82**, 034029 (2010); B.-J. Schaefer and M. Wagner, Phys. Rev. D **85**, 034027 (2012); U. S. Gupta and V. K. Tiwari, Phys. Rev. D **85**, 014010 (2012); R. Khan, J. O. Andersen, L. T. Kyllingstad, and M. Khan, Int. J. Mod. Phys. A **31**, 1650025 (2016).

[38] C. Wetterich, Phys. Lett. B **301**, 90 (1993).

[39] J. Berges, N. Tetradis, and C. Wetterich, Phys. Lett. B **393**, 387 (1997); J. M. Pawlowski, Ann. Phys. (Amsterdam) **322**, 2831 (2007); J. Braun, J. Phys. G **39**, 033001 (2012); H. Gies, Lect. Notes Phys. **852**, 287 (2012); B.-J. Schaefer and J. Wambach, Phys. Part. Nucl. **39**, 1025 (2008).

[40] J. Braun, M. Leonhardt, and J. M. Pawlowski, SciPost Phys. **6**, 056 (2019).

[41] D. F. Litim, Phys. Rev. D **64**, 105007 (2001); D. F. Litim and J. M. Pawlowski, J. High Energy Phys., 11 (2006) 026.

[42] T. D. Cohen, Phys. Rev. Lett. **91**, 222001 (2003).

[43] B.-J. Schaefer, J. M. Pawlowski, and J. Wambach, Phys. Rev. D **76**, 074023 (2007).

[44] S. Roessner, C. Ratti, and W. Weise, Phys. Rev. D **75**, 034007 (2007).

[45] K. Fukushima, Phys. Rev. D **77**, 114028 (2008).

[46] T. K. Herbst, J. M. Pawlowski, and B.-J. Schaefer, Phys. Lett. B **696**, 58 (2011).

[47] T. K. Herbst, M. Mitter, J. M. Pawlowski, B.-J. Schaefer, and R. Stiele, Phys. Lett. B **731**, 248 (2014).

[48] O. Ivanytskyi, M. A. Perez-Garcia, V. Sagun, and C. Albertus, Phys. Rev. D **100**, 103020 (2019).

[49] K. Fukushima and V. Skokov, Prog. Part. Nucl. Phys. **96**, 154 (2017).

[50] W.-j. Fu, J. M. Pawlowski, and F. Rennecke, SciPost Phys. Core **2**, 002 (2020); F. Rennecke and B.-J. Schaefer, Phys. Rev. D **96**, 016009 (2017).

[51] R.-A. Tripolt, B.-J. Schaefer, L. von Smekal, and J. Wambach, Phys. Rev. D **97**, 034022 (2018).

[52] B.-J. Schaefer and J. Wambach, Nucl. Phys. **A757**, 479 (2005).

[53] N. K. Glendenning, Phys. Rev. D **46**, 1274 (1992).

[54] F. Gulminelli and A. R. Raduta, Phys. Rev. C **92**, 055803 (2015); P. Danielewicz and J. Lee, Nucl. Phys. **A818**, 36 (2009); E. Chabanat, P. Bonche, P. Haensel, J. Meyer, and R. Schaeffer, Nucl. Phys. **A635**, 231 (1998).

[55] S. Typel, G. Ropke, T. Klahn, D. Blaschke, and H. H. Wolter, Phys. Rev. C **81**, 015803 (2010); M. Hempel and J. Schaffner-Bielich, Nucl. Phys. **A837**, 210 (2010).

[56] A. W. Steiner, M. Hempel, and T. Fischer, Astrophys. J. **774**, 17 (2013).

[57] I. Bombaci and D. Logoteta, Astron. Astrophys. **609**, A128 (2018).

[58] G. Baym, S. Furusawa, T. Hatsuda, T. Kojo, and H. Togashi, Astrophys. J. **885**, 42 (2019).

[59] M. Alford and A. Sedrakian, Phys. Rev. Lett. **119**, 161104 (2017).

[60] S. Typel, M. Oertel, and T. Klähn, Phys. Part. Nucl. **46**, 633 (2015).

[61] M. G. Alford, S. Han, and M. Prakash, Phys. Rev. D **88**, 083013 (2013).

[62] S. Benic, D. Blaschke, D. E. Alvarez-Castillo, T. Fischer, and S. Typel, Astron. Astrophys. **577**, A40 (2015).

[63] I. Tews, J. Carlson, S. Gandolfi, and S. Reddy, Astrophys. J. **860**, 149 (2018).

[64] P. Bedaque and A. W. Steiner, Phys. Rev. Lett. **114**, 031103 (2015).

[65] S. Borsanyi, G. Endrodi, Z. Fodor, S. D. Katz, S. Krieg, C. Ratti, and K. K. Szabo, J. High Energy Phys. 08 (2012) 053.

[66] P. Benincasa and A. Buchel, Phys. Lett. B **640**, 108 (2006).

[67] A. Cherman, T. D. Cohen, and A. Nellore, Phys. Rev. D **80**, 066003 (2009).

[68] C. Ecker, C. Hoyos, N. Jokela, D. R. Fernández, and A. Vuorinen, J. High Energy Phys. 11 (2017) 031.

[69] Z.-Y. Zhu, E.-P. Zhou, and A. Li, Astrophys. J. **862**, 98 (2018).

[70] M. A. Aloy, J. M. Ibáñez, N. Sanchis-Gual, M. Obergaulinger, J. A. Font, S. Serna, and A. Marquina, Mon. Not. R. Astron. Soc. **484**, 4980 (2019).

[71] R. C. Tolman, Phys. Rev. **55**, 364 (1939); J. R. Oppenheimer and G. M. Volkoff, Phys. Rev. **55**, 374 (1939).

[72] J. Braun, M. Leonhardt, and M. Pospiech, Phys. Rev. D **96**, 076003 (2017); M. Mitter, J. M. Pawlowski, and N. Strodthoff, Phys. Rev. D **91**, 054035 (2015).

[73] W.-j. Fu, J. M. Pawlowski, and F. Rennecke, Phys. Rev. D **101**, 054032 (2020); W.-j. Fu, J. M. Pawlowski, F. Rennecke, and B.-J. Schaefer, Phys. Rev. D **94**, 116020 (2016); J. Braun, L. Fister, J. M. Pawlowski, and F. Rennecke, Phys. Rev. D **94**, 034016 (2016).

[74] M. G. Alford, A. Schmitt, K. Rajagopal, and T. Schafer, Rev. Mod. Phys. **80**, 1455 (2008).

[75] K. Fukushima and T. Hatsuda, Rep. Prog. Phys. **74**, 014001 (2011).

[76] R. Storn and K. Price, J. Global Optim. **11**, 341 (1997).

[77] S. Carignano, M. Buballa, and B.-J. Schaefer, Phys. Rev. D **90**, 014033 (2014).

[78] E. Grossi and N. Wink, arXiv:1903.09503; J. Borchardt and B. Knorr, Phys. Rev. D **94**, 025027 (2016).